Author Manuscript
Author Manuscript
Author Manuscript
Author Manuscript

HHS Public Access
Author manuscript
Nanoscale. Author manuscript; available in PMC 2020 May 16.

Published in final edited form as:
Nanoscale. 2019 May 16; 11(19): 9760–9768. doi:10.1039/c9nr02065a.

Polydopamine-decorated Tobacco Mosaic Virus for Photoacoustic/Magnetic Resonance Bimodal Imaging and Photothermal Cancer Therapy

He Hu[a,e,*], **Qi Yang**[f], **Simona Baroni**[g], **Hong Yang**[f], **Silvio Aime**[g], **Nicole F. Steinmetz**[a,b,c,d,e,*]

[a]Department of NanoEngineering, University of California-San Diego, 9500 Gilman Dr., La Jolla, CA 92093, USA

[b]Department of Radiology, University of California-San Diego, 9500 Gilman Dr., La Jolla, CA 92093, USA

[c]Department of Bioengineering, University of California-San Diego, 9500 Gilman Dr., La Jolla, CA 92093, USA

[d]Moores Cancer Center, University of California-San Diego, 9500 Gilman Dr., La Jolla, CA 92093, USA

[e]Department of Biomedical Engineering, Case Western Reserve University Schools of Medicine and Engineering, 10900 Euclid Ave., Cleveland, OH 44106, USA

[f]Department of Chemistry, Shanghai Normal University, 100 Guilin Rd., Shanghai, China

[g]Department of Molecular Biotechnologies and Health Sciences, University of Torino, Via Nizza, 52, Torino, 10126, Italy

Abstract

Nanotheranostic reagents that integrate magnetic resonance imaging (MRI) and photothermal therapy (PTT) offer a promising strategy for the treatment of human disease. However, classic gadolinium (Gd)-based T_1-MRI contrast agents are limited by their low relaxivity. To address this, we produced Gd-loaded Tobacco mosaic virus (TMV) particles coated with the mussel-inspired biopolymer polydopamine (PDA). Such biocompatible nanotheranostic reagents can be used to facilitate PTT, guided by multimodal magnetic resonance/photoacoustic imaging. The r_1-relaxivity of the Gd-TMV-PDA particles at 60 MHz was ~80 $mM^{-1}s^{-1}$, compared to 13.63 $mM^{-1}s^{-1}$ for the uncoated Gd-TMV particles. The Gd-TMV-PDA particles also promoted strong near-infrared absorption with high photothermal conversion efficiency (28.9%) and demonstrated excellent photoacoustic contrast. Multimodal imaging and PTT resulted in the effective killing of PC-3 prostate cancer cells. Gd-TMV-PDA nanoparticles therefore offer a promising theranostic approach that can now be tested *in vivo* in cancer models.

Graphical Abstract

*Corresponding authors: Prof. Nicole F. Steinmetz: nsteinmetz@ucsd.edu, Dr. He Hu: h7hu@eng.ucsd.edu.

Supporting Information
The detail experiment section in Supporting Information is available from Online or from the author.

Author Manuscript Author Manuscript Author Manuscript Author Manuscript

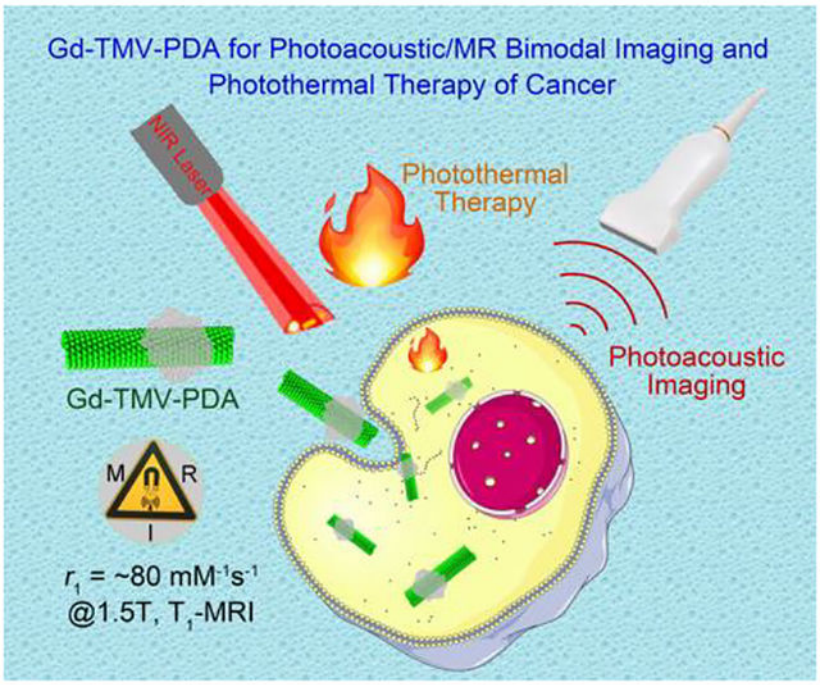

The Gd-TMV-PDA nanotheranostic reagents demonstrated highly r_1-relaxivity of ~80 mM^{-1}s^{-1} at 60 MHz, strong near-infrared absorption with high photothermal conversion efficiency (28.9%), excellent photoacoustic contrast and good biocompatibility.

Keywords

Biopolymer; multimodal imaging; image-guided therapy; nanotheranostics; heterogeneous nanostructure

1. Introduction

Multimodal image-guided therapy is a promising strategy to pinpoint lesion sites, facilitate drug delivery, and monitor therapeutic responses.[1] A nanotheranostic (one-for-all) agent combines multimodal imaging with the delivery of drugs, immunomodulators, gene vectors, or photothermal/photodynamic reagents in a single formulation.[2, 3] Various imaging modalities can be used, including magnetic resonance imaging (MRI) and photoacoustic (PA) imaging. MRI is a powerful noninvasive imaging method with high spatial and temporal resolution and excellent soft tissue contrast.[4] PA imaging is a more recent development based on the photoacoustic effect, which relies on the detection of acoustic waves generated by biological targets following the absorption of light. Within living tissues, light is scattered ~1000-fold more effectively than ultrasound, so acoustic waves penetrate tissues to a greater depth (at least 5.2 cm) than optical imaging modalities (< 3 cm) and achieve better sensitivity and resolution.[5–7]

Photothermal therapy (PTT) is an encouraging noninvasive therapeutic strategy for treatment of cancer, in which near-infrared (NIR) photo-absorbers generate heat when exposed to NIR

Author Manuscript Author Manuscript Author Manuscript Author Manuscript

light from a laser, resulting in the specific and precise thermal ablation of cancer cells.[8, 9] The integration of MRI and PA imaging with PTT into a single nanotheranostic reagent for double image-guided therapy would offer at least three key advantages. First, the spatial resolution and soft tissue contrast of MRI would complement the sensitive three-dimensional structural images generated by PA imaging to pinpoint the location of lesions precisely.[10] Second, the MR/PA imaging combination would provide insight into the microenvironment and metastatic potential of tumors.[11] Third, MR/PA image-guided PTT in clinical trials would allow therapeutic responses to be monitored, providing information more rapidly than traditional endpoint trials and allowing physicians to adjust the therapeutic regimen in real time.[12]

There are several challenges that must be addressed before these goals are achieved. For example, MRI suffers from relatively low sensitivity.[13] Various of MRI contrast agents have been developed to alter the longitudinal (T_1) or transverse (T_2) relaxation times of the surrounding water protons thus increasing the contrast between target lesions and the background to improve the sensitivity of MRI for clinical diagnosis.[13] Gadolinium(III) ions (Gd^{3+}) in chelator complexes such as DOTA (monoamide-1,4,7,10-tetraazacyclododecane-N-N′-N″-N‴-tetraacetic acid) form suitable contrast agents that shorten T_1 in low-strength magnetic fields (≤1.5 T), which are used in more than 30% of clinical MRI scans.[13] However, these Gd-based contrast agents suffer from poor longitudinal relaxivity (r_1), which rapidly decreases with increasing field strength and thus limits their effectiveness during MRI.[14, 15] Research has therefore focused on the development of contrast agents with high r_1-relaxivity, which are compatible with higher-field-strength MRI scanners.

Recent reports highlighted the application of plant virus nanoparticles and virus like nanoparticles for design of high relaxivity MRI contrast agent. This includes the development of Gd-hydroxypyridonate-modified MS2 nanoparticles with r_1 of 41.6 $mM^{-1}s^{-1}$ at 30 MHz[16] and 38.2 $mM^{-1}s^{-1}$ at 60 MHz,[17] respectively. Gd-DOTA-loaded cowpea mosaic virus (CPMV) nanoparticles,[18] as well as metal-free Tobacco mosaic virus (TMV) with paramagnetic organic radical compounds have been reported; the latter serves as MRI and electron paramagnetic resonance (EPR) contrast agent.[19] Furthermore, we have previously demonstrated that the conjugation of T_1-Gd-DOTA[20] or T_2-Dy-DOTA[21] complexes to nanotube-like TMV nanoparticles can dramatically increase r_1 and r_2 values, respectively. TMV is a plant virus with a capsid comprising 2130 identical coat proteins that self-assemble into a 300 × 18 nm hollow tube with a 4 nm wide solvent-accessible internal channel containing the single-stranded genomic RNA.[22] The benefits of such tube-like particles including more effective evasion of the immune system, particularly the mononuclear phagocyte system, and more efficient margination toward the blood vessel wall to improve extravasation.[23, 24] Importantly, TMV is biocompatible and biodegradable and does not cause infections in humans.[25] Therefore, the development of Gd-DOTA-conjugated multimodal imaging agents based on TMV has potential to optimize MRI and other imaging modalities.

Biocompatibility and photothermal conversion efficiency are the most challenging aspects for the development of effective PTT agents.[8, 9] Plasmonic metal nanoparticles such as Ag[26], Au[27–29] and Pt[30], carbon nanomaterials such as graphene[31] and carbon nanotubes[32],

Author Manuscript Author Manuscript Author Manuscript Author Manuscript

and minerals such as iron oxide[33] and copper selenide[34, 35] have been widely used as PTT agents for preclinical research, the biocompatibility of such modalities is low.[12] In contrast, polydopamine (PDA) is a melanin-like mimic of mussel adhesion proteins, which shows excellent photothermal stability, biocompatibility and biodegradability.[36, 37] PDA is easily produced by the self-polymerization of dopamine in a mild reaction environment, and the unique chemical structure makes it feasible to coat other kinds of particles or to modify the coating with functional groups.[37]

We therefore hypothesized that the combination of PDA and Gd-loaded TMV would be an ideal platform for nanotheranostic reagents with excellent MRI, PA imaging, and PTT capabilities. However, heterogeneous protein-based nanoparticles are difficult to synthesize, and the few previous successes have mainly involved protein-inorganic hybrid nanoparticles[38, 39] rather than biopolymer-coated heterogeneous protein nanostructures.[40] We are aware of only one previous report concerning the preparation of hybrid PDA/TMV nanofibers, but these were used to seed gold nanoparticles[41] and no studies have described the use of modified TMV for multimodal imaging to guide PTT.[38, 40] Here, we loaded TMV with Gd-DOTA on the internal surface, and then coated the Gd-TMV particles with PDA by the *in situ* self-polymerization of dopamine on the external surface. The coating reaction was optimized to obtain monodisperse Gd-TMV-PDA nanotheranostic particles, which were systematically tested for their compatibility with MRI, PA imaging and PTT.

2. Results and discussion

2.1 Synthesis of Gd-TMV-PDA and characterization

TMV nanoparticles were propagated in and isolated from *Nicotiana benthamiana* plants, which are inexpensive to grow and highly scalable.[42] The high-resolution crystal structure of TMV (Fig. 1A1) includes an internal glutamic acid residue (GLU97/106, blue) and an external tyrosine residue (TYR139, red) that can be functionalized using the well-established copper-catalyzed azide-alkyne cycloaddition (CuAAC) strategy, also known as click chemistry.[20, 42] The internal TMV surface was modified with alkyne groups then conjugated with the macrocyclic T_1-MRI contrast agent Gd-DOTA-azide *via* a click reaction.

Both native TMV and Gd-TMV (2 mg) were coated with PDA by *in situ* self-polymerization with dopamine under the same conditions, varying the dopamine dose in the range 2.5–7 mg. The morphology of the particles after each modification step was observed by transmission electron microscopy (TEM). The native TMV nanoparticles showed the typical elongated nanostructure (Fig. 1B1) and a clean, smooth external surface (Fig. 1B2). After internal chemical conjugation with Gd-DOTA, the Gd-TMV particles (Fig. 1E1–2) retained the shape and morphology of the native TMV particles. When the native TMV particles (2 mg) were coated with PDA using 2.5 mg dopamine, the particles were homogenously coated but remained discrete (Fig. 1C1–2). In contrast, at the higher dose of 3.5 mg dopamine, the PDA coat was thicker and longer with thorn-like protuberances, and the particles tended to aggregate (Fig. 1D1–2). Interestingly, increasing the dopamine dose from 2.5 to 7 mg caused significant changes to the PDA coating on the Gd-TMV particle surface, with knot-like protrusions 10~40 nm in depth forming at dopamine doses of 2.5 (Fig. 1F), 3.5 (Fig. 1G), and 5 mg (Fig. 1H), but both a full coating and knots at the highest dose of 7 mg (Fig. 1I).

Author Manuscript Author Manuscript Author Manuscript Author Manuscript

Generally, the knot-like PDA deposits preferentially formed on the ends of the particles but more appeared on the body as the dopamine dose increased. Similar results were reported previously for the PDA-coated TMV used to grow gold nanoparticles under acidic conditions.[41] We concluded that Gd-TMV-PDA particles with a consistent morphology could be prepared using 2.5–3.5 mg dopamine, and we used the Gd-TMV-PDA sample prepared with 3.5 mg dopamine for all further characterizations and applications.

2.2 Longitudinal relaxivity of Gd-TMV-PDA and MRI of cancer cells

The longitudinal relaxivity (r_1) of the Gd-TMV-PDA nanoparticles was measured in different magnetic fields (1.5, 7.0 and 9.4 T) as shown in Fig. 2A–B. The r_1 values of the Gd-TMV particles (per Gd^{3+}) were 13.63, 5.75 and 5.25 $mM^{-1}s^{-1}$ at 1.5, 7 and 9.4 T, respectively (Fig. 2A), corresponding to per particle values of ~20,613, 8696 and 7940 $mM^{-1}s^{-1}$ at 1.5, 7 and 9.4 T, respectively. The r_1 values of the Gd-TMV particles agreed with previous reports describing these contrast agents[20], and were higher than the values of commercial T_1 MRI contrast agents (3–5 $mM^{-1}s^{-1}$).[15] Interestingly, after PDA coating, the r_1 values dramatically increased to 79.85, 15.02 and 10.09 $mM^{-1}s^{-1}$ (per Gd^{3+}) at 1.5, 7.0 and 9.4 T, respectively, corresponding to per particle values of ~120,757, 22,715 and 15,260 $mM^{-1}s^{-1}$ at 1.5, 7.0 and 9.4 T, respectively (Fig. 2B). Gd-TMV-PDA particles therefore appear to achieve among the highest r_1 values compared to either analogue protein-based nanostructures or inorganic nanoparticles under similar conditions. For example, the longitudinal relaxivity values of our Gd-TMV-PDA particles were ~4-fold higher than Gd-P22 (21.7 $mM^{-1}s^{-1}$) at 28 MHz,[43] almost ~5-fold higher than Gd-MS2 (16.9 $mM^{-1}s^{-1}$)[44] and Gd-CPMV (15.5 $mM^{-1}s^{-1}$)[18] at ~64 MHz, ~2.5-fold higher than Gd-MS2 in ultra-high-strength magnetic fields (4.3 $mM^{-1}s^{-1}$ at 9.4 T), and ~3-fold higher than mesoporous silica[45, 46] and polymer nanoparticles[47, 48]. The longitudinal relaxivities of these functionalized nanoparticles are compared in Table S1.

To demonstrate the suitability of the new contrast agents for ultra-high-field MRI (UHFMRI), we obtained concentration-dependent T_1-mapping phantom images of the Gd-TMV-PDA water solutions at 7.0 and 9.4 T (Fig. 2D), and compared them to the Gd-TMV phantoms (Fig. 2C). The T_1-mapping images of Gd-TMV-PDA showed a clear Gd^{3+} concentration-dependent positive contrast gradient from 0 to 79.5 μM (158.7 μM in Gd-TMV). Gd-TMV-PDA therefore achieved higher contrast efficiency than Gd-TMV but only required 50% of the Gd^{3+} concentration in each phantom compared to Gd-TMV.

An increase in the relaxivity of Gd-based contrast agents can be achieved by optimizing the exchange rate τ_M (in the order of nanoseconds) for the metal-coordinated water molecules, and the rotational correlation times (τ_R) for the metal complex.[14, 15] Such strategies can be realized by immobilizing the Gd-complex on nanostructured materials, slowing down their molecular tumbling while maintaining the water residence time.[14, 15] We therefore carried out a thorough relaxometric characterization of the Gd-TMV-PDA particles by measuring the nuclear magnetic relaxation dispersion (NMRD) profiles of Gd-TMV and Gd-TMV-PDA over the frequency range 0.1–70 MHz at 25°C (Fig. 2E). The NMRD profiles were identical, with a relaxivity peak centered on 40 MHz indicating slowly tumbling systems.[46] Therefore, the dramatically increased longitudinal relaxivity of Gd-TMV-PDA compared to Gd-TMV

Author Manuscript Author Manuscript Author Manuscript Author Manuscript

could reflect two major factors. First, the PDA coating may increase the rigidity of the Gd-DOTA complex, increasing the τ_R value.[49] Alternatively, given that water molecules inside carbon nanotubes experience extremely high flow velocities,[50, 51] PDA with its abundant hydroxyl groups may present more hydrophilic residues to bind water molecules with access to Gd-DOTA resulting in faster exchange between Gd-coordinated internal water and bulk water. Notably, the relaxivity peak of most T_1 contrast agents centers on ~21 MHz, and the greater peak shift revealed by our particles in higher-strength magnetic fields confirms their suitability for UHFMRI.

Finally, to evaluate the ability of the particles to detect cancer cells by UHFMRI, the prostate cancer cell line PC-3 was incubated for 3 h at 37°C with different concentrations of Gd-TMV-PDA (0.1, 0.2, 0.3 0.4 and 0.5 mg/mL) and then the cells were immobilized in agarose. A T_1-mapping MRI scan revealed that the nanoparticles reduced the normalized T_1 value in a concentration-dependent manner (Fig. 2F). The quantity of Gd^{3+} taken up by PC-3 cells per mg protein was determined by ICP-OES and the Bradford protein assay, revealing a concentration-dependent range of 58.3–82.1 pmol Gd^{3+}/mg protein for the Gd-TMV-PDA nanoparticles. These particles were passively taken up by cancer cells in a relatively efficient manner, consistent with earlier reports showing that elongated nanoparticles can pass through cell membranes more effectively than spherical nanoparticles due to their high degree of nanoparticle-to-cell contacts.[23, 24]

2.3 PTT properties of Gd-TMV-PDA and cancer cell killing profiles

Next, we investigated the photothermal properties and *in vitro* cytotoxicity of the Gd-TMV-PDA particles (Fig. 3). The particles exhibited a broad absorption range (600–1000 nm) as shown by the absorption spectra (Fig. 3A). The absorbance at 808 nm was linearly correlated with the concentration of the particles (Fig. S3). The heat generated by different concentrations of Gd-TMV-PDA (50, 100, 200, 400, 500 and 667 μg/mL) was monitored using a near-infrared (NIR) camera to record the temperature profile in response to irradiation with an 808 nm NIR laser (1 W/cm^2) for 5 min (Fig. 3B). The Gd-TMV-PDA solution underwent rapid heating during irradiation, with the temperature rise dependent on the particle concentration and the duration of the laser pulse, indicating that heat generation can be finely tuned. After 5 min, the temperature of the 50, 100, 200, 400, 500 and 667 μg/m Gd-TMV-PD solutions increased from room temperature (25°C) to 28.8, 30.6, 33.4, 37.8, 40.4 and 44.1°C, respectively. The PBS control solution did not increase in temperature when exposed to the same stimulus. We also investigated the thermal effect of a 667 μg/mL Gd-TMV-PD solution irradiated with the 808-nm laser at different power densities ranging from 0.4 to 1 W/cm^2 (Fig. 3C). The change in temperature ranged from 7.4 to 19.1°C depending on the laser power. Based on these data, the photothermal conversion efficiency of the Gd-TMV-PDA particles was calculated,[52, 53] yielding a value of 28.9%. This is similar to the efficiency of widely-used photothermal agents such as Fe@Fe_3O_4 (24.4%),[53] gold nanocages (13%),[27] gold nanorods (21%),[28] and $Cu_{2-x}Se$ (22%).[34] To confirm the stability of the Gd-TMV-PDA particles after laser irradiation, we observed the morphology by TEM, tracked the particles size by dynamic light scattering (DLS) (Fig. S4) and monitored the absorption spectra of the Gd-TMV-PDA solution after before and after irradiation (Fig. 3A). There were no obvious differences in absorption or particle

Author Manuscript Author Manuscript Author Manuscript Author Manuscript

morphology, indicating that the particles are photothermally stable. The stock solution of 200 μg/mL Gd-TMV-PDA remained homogeneous after irradiation (Fig. 3A, inset). Moreover, after eight cycles of laser irradiation, the laser-induced temperature increases in the solution were unchanged (Fig. 3E). In contrast, gold nanorods change into cross-linked nanowires following laser irradiation, causing the absorption peak in the NIR region (and the red color) to disappear, and a gradual decline in the temperature increase during irradiation.[53] These data show that Gd-TMV-PDA particles benefit from both high photothermal conversion efficiency and high photothermal stability.

To confirm that Gd-TMV-PDA particles can be used as photothermal agents to kill cancer cells, we conducted a fluorescence-based live/dead cell assay and directly visualized the cytotoxicity of Gd-TMV-PDA particles towards human PC-3 prostate cancer cells by confocal laser scanning microscopy (CLSM). Following laser irradiation (808 nm, 1 W/cm^2), the PC-3 cells were simultaneously stained with calcein-AM and propidium iodide (PI) to distinguish live cells (green fluorescence) from dead ones (red fluorescence). As shown in Fig. 3F, the proportion of dead PC-3 cells was dependent on the duration of laser irradiation. Compared with the cells that were not irradiated, significant red fluorescence was observed 3 min after irradiation, and the tumor cells were killed completely within 5 min. The photothermal ablation efficacy of Gd-TMV-PDA was confirmed by trypan blue staining and cytotoxicity MTT assays (Fig. S5). In the three control groups (PC-3 cells alone, PC-3 cells cultured with Gd-TMV-PDA (500 μg/mL) without irradiation, and PC-3 cells irradiated (1 W/cm^2 in the absence of Gd-TMV-PDA), we observed hardly any dead cells. However, nearly all the PC-3 cells incubated with Gd-TMV-PDA and exposed to the laser were stained blue, indicating the ablation of cancer cells consistent with the results of the calcein-AM/PI assay. Therefore, both assays confirmed the powerful thermal cytotoxicity of Gd-TMV-PDA towards cancer cells. We also confirmed PTT efficacy using the 4T1 cell line derived from mice and serving as a model for aggressive breast cancer which showed similar results as PC-3 (Fig. S5).

2.4 PA properties of Gd-TMV-PDA

Given the excellent photothermal properties of the Gd-TMV-PDA particles, next we investigated its PA characteristics because photothermal and PA behaviors are always associated.[9] A solution of Gd-TMV-PDA particles (200 μg/mL, aqueous solution) emitted clear PA signals following irradiation with a pulsed laser in the wavelength range 680–900 nm (Fig. 4A). Stronger signals were produced at shorter incident wavelengths, which is consistent with the absorption properties of Gd-TMV-PDA (Fig. 3A). The PA imaging phantoms of several concentrations of Gd-TMV-PDA (50–300 μg/mL) in PBS were scanned, yielding clear and homogenous images with a linear relationship between the signal and the concentration of Gd-TMV-PDA (Fig. 4B).

3. Experimental

3.1 TMV bioconjugation:

Wild-type TMV nanoparticles were propagated in *N. benthamiana* plants and isolated from plant extracts by chloroform : butanol extraction and ultracentrifugation as previously

Author Manuscript Author Manuscript Author Manuscript Author Manuscript

described.[42] The TMV concentration in plant extracts was determined using a NanoDrop 2000 UV/visible spectrophotometer (Thermo Fisher Scientific, Waltham, MI, USA), assuming a molar extinction coefficient (ε_{260nm}) of ~3.0 $mLmg^{-1}cm^{-1}$. The Gd-TMV nanoparticles were synthesized by carbodiimide coupling (targeting internal glutamic acid residues) to introduce alkyne ligation handles, followed by the introduction of Gd-DOTA as the MRI contrast agent.

3.2 PDA coating:

We diluted 2 mg of TMV or Gd-TMV stock solution in 20 mL Tris buffer (pH 8.5), added 2.5–7 mg dopamine to the solution dropwise while stirring, and allowed the reaction to proceed for 6 h open to the atmosphere. The product was centrifuged at 25,000 *g*, washed with PBS and then with deionized water. The morphology of the particles at each step was observed by transmission electron microscopy using a Tecnai F30 instrument.

3.3 Measurement of r_1-relaxivity and T_1-mapping phantoms:

The Gd^{3+} ionic relaxivity of the particles was tested at 37°C using a Brukman Minispec mq60 relaxometer (60 MHz) and a BioSpec 70/30USR pre-clinical 7.0 T (300 MHz) and 9.4 T (400 MHz) MRI (Bruker Inc., Billerica, MA, USA). NMRD profiles ($1/T_1$) were measured at 25°C in magnetic fields ranging in strength from 0.00024 to 0.47 T (corresponding to 0.01–20 MHz proton Larmor frequency) on a Stelar (Mede, Italy) field-cycling relaxometer, with an absolute uncertainty <1%. Data points from 0.5 T (21.5 MHz) to 1.7 T (70 MHz) were collected on a Stelar Spinmaster spectrometer. The concentration of Gd^{3+} was determined by inductively coupled plasma optical emission spectrometry using a 730-ES ICP-OES device (Agilent Technologies, Santa Clara, CA, USA).

3.4 PC-3 cell culture:

The human prostate cancer cell line PC-3 (ATCC) was maintained at 37°C in a humidified 5% CO_2 atmosphere. The cells were grown in RPMI-1640 medium (Corning Life Sciences, New York, NY, USA) containing 10% fetal bovine serum (Atlanta Biologicals, Flowery Branch, GA, USA) and 1% penicillin–streptomycin (Thermo Fisher Scientific).

3.5 In vitro MRI of PC-3 cells:

Approximately 2×10^5 PC-3 cells were seeded per well into 24-well plates and grown overnight as above. We then added different concentrations of the nanoparticles (0, 0.1, 0.2 0.3 and 0.4 mg/mL, equivalent to 0, 1×10^6, 2×10^6, 3×10^6 and 4×10^6 particles/cell, diluted in PBS) and incubated for a further 3 h. The cells were then washed three times with PBS, detached with trypsin/EDTA, transferred to Falcon tubes and embedded in 25% agarose. The *in vitro* MRI studies were carried out using a horizontal Biospec 7 T scanners (Bruker Inc., Billerica, MA, USA) equipped with a 3-cm birdcage ^1H coil (Bruker, Erlangen, Germany). First, a multi-slice, T_2 weighted imaging sequence (RARE)[54] was used to provide location information about the cells with the following parameters: TE/TR=24/3000 ms, RARE factor = 8, NAV = 1, number of axial slices = 15, slice thickness = 1.5 mm, matrix size = 128 × 128, 30 × 30 mm field of view (FOV). The total acquisition time was 48 s. Next, single-slice T_1-mapping was performed using a saturation-recovery-look-locker (SRLL)

Author Manuscript Author Manuscript Author Manuscript Author Manuscript

sequence as previously described, and a spiral readout to accelerate acquisition.[55] The spiral trajectory required 32 interleaves to fully sample the *k*-space for a FOV of 30 × 30 mm^2 and matrix size of 128 × 128. The spiral SRLL used the following parameters: single slice, FA = 10^0, TE = 3.5 ms, slice thickness = 1.5 mm, NAV = 1. Fifty images that covered 6 s of the saturation recovery curve were acquired at intervals of 120 ms. Proton density (M0) images were acquired with same spiral trajectory and TR = 2000 ms. The spiral trajectory of 32 interleaves with 0th moment compensation was designed using the minimum-time gradient method and measured manually for reconstruction. The scan time for each average was 2 min 40 s. After imaging, the cell samples were collected and sonicated at 30% power for 30 s in ice, and the total protein content was measured using the Quick Start Bradford Protein Assay with bovine serum albumin as standard (Bio-Rad, Hercules, CA, USA). The reset cell samples were then digested with concentrated hot HNO_3 and the Gd content was determined by ICP-OES.

3.6 Photothermal experiments:

The aqueous suspension containing different concentrations of the Gd-TMV-PDA particles (1.5 mL) in a quartz cuvette was irradiated with an 808-nm laser with power settings in the range 0.38–1 W/cm^2 for 500 s. The change in temperature was recorded using an A300 forward-looking infrared (FLIR) thermal camera (FLIR Systems, Wilsonville, OR, USA). The photothermal conversion efficiency of Gd-TMV-PDA was calculated using the equation $\eta = hs(T_{max} - T_{surr}) - Q_{dis} / I(1 - 10^{-A\lambda})$, where h is the thermal conductivity index, s is the surface area of the vessel, T_{max} is the equilibrium temperature during irradiation, T_{surr} is the initial temperature, Q_{dis} is the heat generated by the solvent, I is the power intensity of the laser, and A_λ is the sample's absorption value (here λ = 808 nm).[52, 53]

3.7 Calcein-AM/PI staining:

We seeded 1×10^5 PC-3 cells into 10 × 10 mm plates and cultivated them overnight as described above. Then cells were then incubated with 500 μg/mL Gd-TMV-PDA for 6 h, before washing three times in PBS to remove the excess particles. Different groups of cells were irradiated with the 808-nm laser (1 W/cm^2) for 1, 2, 3, 4, 5 or 10 min. The cells were incubated for a further 2 h then simultaneously stained for 15 min in the dark with calcein-AM and PI as part of the Live/Dead Cytotoxicity Assay Kit (MesGen Shanghai, China). The stained cells were observed on a TCS SP5 inverted microscope (Leica, Wetzlar, Germany) with a 63× oil-immersion objective lens, using 488 and 543 nm lasers to excite calcein-AM and PI, respectively.

3.8 Photoacoustic analysis of Gd-TMV-PDA:

PA imaging was performed with a multispectral optoacoustic tomography (MSOT) scanner (iThera medical, Munich, Germany), was equipped with an array of 128 cylindrically focused transducers to detect PA signals and a tunable pulsed laser (680–980 nm, 10 Hz) to generate the PA effect in polypropylene and Tygon tubes placed across the center of a water bath. The PA spectrum between 680 and 900 nm was measured with an average laser energy density of 40 mJ cm^{-2}. The PA behavior of Gd-TMV-PDA in aqueous solution (50, 100, 150, 200, 250 and 300 μg/mL,) was excited at 680 nm. The intensity was calculated by

Author Manuscript Author Manuscript Author Manuscript Author Manuscript

region of interest analysis on the MSOT imaging system. The PA images were reconstructed using the coherence factor-based sound speed correction method.

4. Conclusions

We have developed a nanotheranostic reagent (Gd-TMV-PDA) for dual modal imaging (MR +PA imaging) and simultaneous PTT for the treatment of cancer. The biopolymer PDA displayed on the Gd-TMV particles dramatically increased the longitudinal relaxivity, while achieving high photothermal conversion efficiency and excellent photoacoustic imaging properties. Our data showed that the Gd-TMV-PDA particles allow the localization of cancer cells by MRI and targeted killing by irradiation with an 808-nm laser in as little as 3 min. Gd-TMV-PDA particles are therefore promising theranostic agents for the precise localization and targeted therapy. We will now move forward with preclinical studies to test the efficacy of Gd-TMV-PDA particles using *in vivo* tumor models.

Supplementary Material

Refer to Web version on PubMed Central for supplementary material.

ACKNOWLEDGMENT:

This work was funded by a grant from the National Institutes of Health (R01CA202814) to NFS.

References:

1. Lee D-E, Koo H, Sun I-C, Ryu JH, Kim K and Kwon IC, Chem. Soc. Rev, 2012, 41, 2656–2672. [PubMed: 22189429]
2. Rieffel J, Chitgupi U and Lovell JF, Small, 2015, 11, 4445–4461. [PubMed: 26185099]
3. Bogart LK, Pourroy G, Murphy CJ, Puntes V, Pellegrino T, Rosenblum D, Peer D and Lévy R, ACS Nano, 2014, 8, 3107–3122. [PubMed: 24641589]
4. Lee H, Shin TH, Cheon J and Weissleder R, Chem. Rev, 2015, 115, 10690–10724. [PubMed: 26258867]
5. Nie L and Chen X, Chem. Soc. Rev, 2014, 43, 7132–7170. [PubMed: 24967718]
6. Wang LV and Hu S, Science, 2012 335, 1458–1462.
7. Miao Q and Pu K, Adv. Mater, 2018, 30, e1801778. [PubMed: 30058244]
8. Vankayala R and Hwang KC, Adv. Mater, 2018, 30, 1706320.
9. Liu Y, Bhattarai P, Dai Z and Chen X, Chem. Soc. Rev, 2019, 48, 2053–2108. [PubMed: 30259015]
10. Tian J, Ding L, Ju H, Yang Y, Li X, Shen Z, Zhu Z, Yu J-S and Yang CJ, Angew. Chem. Int. Ed, 2014, 53, 9544–9549.
11. Kantamneni H, Zevon M, Donzanti MJ, Zhao X, Sheng Y, Barkund SR, McCabe LH, Banach-Petrosky W, Higgins LM, Ganesan S, Riman RE, Roth CM, Tan M-C, Pierce MC, Ganapathy V and Moghe PV, Nat. Biomed. Eng, 2017, 1, 993–1003. [PubMed: 29531851]
12. Lucky SS, Soo KC and Zhang Y, Chem. Rev, 2015, 115, 1990–2042. [PubMed: 25602130]
13. Caravan P, Chem. Soc. Rev, 2006, 35, 512–523. [PubMed: 16729145]
14. Leone L, Ferrauto G, Cossi M, Botta M and Tei L, Front. Chem, 2018, 6, 158. [PubMed: 29868561]
15. Helm L, Future Med. Chem, 2010, 2, 385–396. [PubMed: 21426173]
16. Datta A, Hooker JM, Botta M, Francis MB, Aime S and Raymond KN, J. Am. Chem. Soc, 2008, 130, 2546–2552. [PubMed: 18247608]

Author Manuscript Author Manuscript Author Manuscript Author Manuscript

17. Garimella PD, Datta A, Romanini DW, Raymond KN and Francis MB, J. Am. Chem. Soc, 2011, 133, 14704–14709. [PubMed: 21800868]
18. Prasuhn JDE, Yeh RM, Obenaus A, Manchester M and Finn MG, Chem. Commun, 2007, 1269–1271.
19. Dharmarwardana M, Martins AF, Chen Z, Palacios PM, Nowak CM, Welch RP, Li S, Luzuriaga MA, Bleris L, Pierce BS, Sherry AD and Gassensmith JJ, Mol. Pharmaceutics, 2018, 15, 2973–2983.
20. Bruckman MA, Jiang K, Simpson EJ, Randolph LN, Luyt LG, Yu X and Steinmetz NF, Nano Lett, 2014, 14, 1551–1558. [PubMed: 24499194]
21. Hu H, Zhang Y, Shukla S, Gu Y, Yu X and Steinmetz NF, ACS Nano, 2017, 11, 9249–9258. [PubMed: 28858475]
22. Culver JN, Annu. Rev. Phytopathol, 2002, 40, 287–308. [PubMed: 12147762]
23. Doshi N, Prabhakarpandian B, Rea-Ramsey A, Pant K, Sundaram S and Mitragotri S, J. Control. Release, 2010, 146, 196–200. [PubMed: 20385181]
24. Vácha R, Martinez-Veracoechea FJ and Frenkel D, Nano Lett, 2011, 11, 5391–5395. [PubMed: 22047641]
25. Gulati NM, Pitek AS, Czapar AE, Stewart PL and Steinmetz NF, J. Mater. Chem. B, 2018, 6, 2204–2216. [PubMed: 30294445]
26. Le Ouay B and Stellacci F, Nano Today, 2015, 10, 339–354.
27. Wang Y, Black KCL, Luehmann H, Li W, Zhang Y, Cai X, Wan D, Liu S-Y, Li M, Kim P, Li Z-Y, Wang LV, Liu Y and Xia Y, ACS Nano, 2013, 7, 2068–2077. [PubMed: 23383982]
28. Vankayala R, Huang Y-K, Kalluru P, Chiang C-S and Hwang KC, Small, 2013, 10, 1612–1622. [PubMed: 24339243]
29. Benjamin CE, Chen Z, Kang P, Wilson BA, Li N, Nielsen SO, Qin Z and Gassensmith JJ, J. Am. Chem. Soc, 2018, 140, 17226–17233. [PubMed: 30452248]
30. Erika P, Samuel L, Hynd R, Noriko U, Katsumi K, Yoshiya F, Claude Le S and Sandrine L, Nanotechnology, 2010, 21, 085103.
31. Robinson JT, Tabakman SM, Liang Y, Wang H, Sanchez Casalongue H, Vinh D and Dai H, J. Am. Chem. Soc, 2011, 133, 6825–6831. [PubMed: 21476500]
32. Kam NWS, O'Connell M, Wisdom JA and Dai H, Proc. Natl. Acad. Sci. U. S. A 2005, 102, 11600–11605. [PubMed: 16087878]
33. Zhang X, Xu X, Li T, Lin M, Lin X, Zhang H, Sun H and Yang B, ACS Appl. Mater. Interfaces, 2014, 6, 14552–14561. [PubMed: 25134068]
34. Hessel CM, Pattani VP, Rasch M, Panthani MG, Koo B, Tunnell JW and Korgel BA, Nano Lett, 2011, 11, 2560–2566. [PubMed: 21553924]
35. Goel S, Chen F and Cai W, Small, 2014, 10, 631–645. [PubMed: 24106015]
36. Lee H, Dellatore SM, Miller WM and Messersmith PB, Science, 2007, 318, 426–430. [PubMed: 17947576]
37. Liu Y, Ai K and Lu L, Chem. Rev, 2014, 114, 5057–5115. [PubMed: 24517847]
38. Li F and Wang Q, Small, 2013, 10, 230–245. [PubMed: 23996911]
39. Bruckman MA, Randolph LN, Gulati NM, Stewart PL and Steinmetz NF, J. Mater. Chem. B, 2015, 3, 7503–7510. [PubMed: 26659591]
40. Steinmetz NF and Manchester M, VNPs as templates for materials synthesis, Pan Stanford Publishing Pte. Ltd., 2011.
41. Zhou Q, Liu X, Tian Y, Wu M and Niu Z, Langmuir, 2017, 33, 9866–9872. [PubMed: 28849937]
42. Bruckman MA and Steinmetz NF, in Virus Hybrids as Nanomaterials: Methods and Protocols, eds. Lin B and Ratna B, Humana Press, Totowa, NJ, 2014, DOI: 10.1007/978-1-62703-751-8_13, pp. 173–185.
43. Qazi S, Liepold LO, Abedin MJ, Johnson B, Prevelige P, Frank JA and Douglas T, Mol. Pharmaceutics, 2013, 10, 11–17.
44. Anderson EA, Isaacman S, Peabody DS, Wang EY, Canary JW and Kirshenbaum K, Nano Lett, 2006, 6, 1160–1164. [PubMed: 16771573]

Author Manuscript Author Manuscript Author Manuscript Author Manuscript

45. Carniato F, Tei L, Cossi M, Marchese L and Botta M, Chem. Eur. J, 2010, 16, 10727–10734. [PubMed: 20669190]
46. Hu H, Arena F, Gianolio E, Boffa C, Di Gregorio E, Stefania R, Orio L, Baroni S and Aime S, Nanoscale, 2016, 8, 7094–7104. [PubMed: 26960989]
47. Huang C-H, Nwe K, Al Zaki A, Brechbiel MW and Tsourkas A, ACS Nano, 2012, 6, 9416–9424. [PubMed: 23098069]
48. Ratzinger G, Agrawal P, Koner W, Lonkai J, Sanders HMHF, Terreno E, Wirth M, Strijkers GJ, Nicolay K and Gabor F, Biomaterials, 2010, 31 8716–8723. [PubMed: 20797782]
49. Wang Z, Carniato F, Xie Y, Huang Y, Li Y, He S, Zang N, Rinehart JD, Botta M and Gianneschi NC, Small, 2017, 13, 1701830.
50. Joseph S and Aluru NR, Nano Lett, 2008, 8, 452–458. [PubMed: 18189436]
51. Striolo A, Nano Lett, 2006, 6, 633–639. [PubMed: 16608257]
52. Liu Y, Ai K, Liu J, Deng M, He Y and Lu L, Adv. Mater, 2013, 25, 1353–1359. [PubMed: 23280690]
53. Zhou Z, Sun Y, Shen J, Wei J, Yu C, Kong B, Liu W, Yang H, Yang S and Wang W, Biomaterials, 2014, 35, 7470–7478. [PubMed: 24881997]
54. Chen Y, Li W, Jiang K, Wang CY and Yu X, J. Magn. Reson. Imaging, 2016, 44, 375–382. [PubMed: 26854752]
55. Li W, Griswold M and Yu X, Magn. Reson. Med, 2010, 64, 1296–1303. [PubMed: 20632410]

Author Manuscript Author Manuscript Author Manuscript Author Manuscript

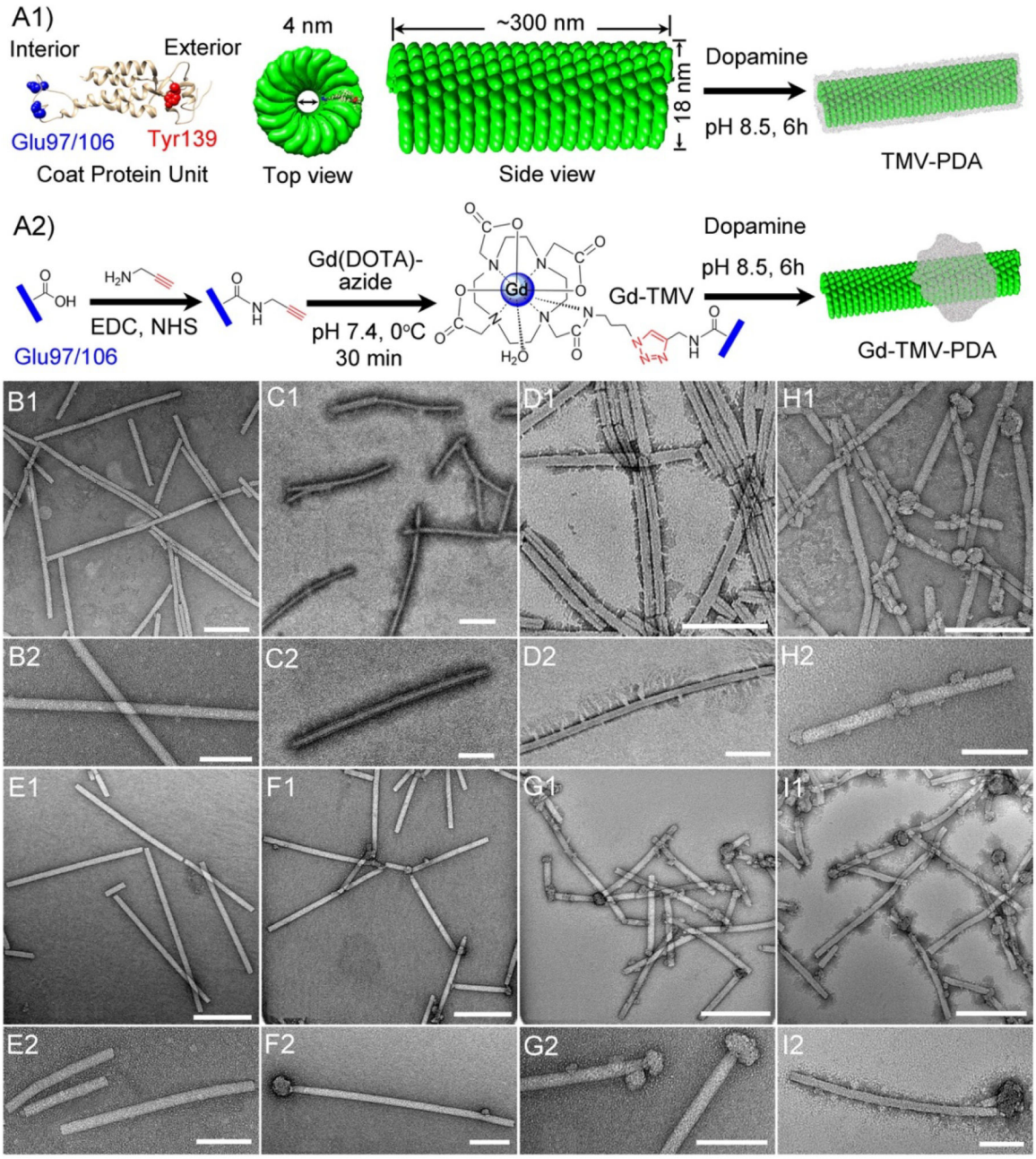

Fig. 1.

(A1) Structure of the Tobacco mosaic virus (TMV) coat protein, showing the surface-exposed internal glutamic acid (blue) and external tyrosine (red) residues, and the structure of the assembled wild-type capsid coated with polydopamine (TMV-PDA). (A2) Strategy for internal loading of Gd-DOTA (Gd-TMV) and partial decoration with PDA (Gd-TMV-PDA). Images were created using UCSF Chimera software, PDB entry 2TMV and ChemDraw v15.0. Transmission electron micrographs (TEM) of (B1–2) native wild-type TMV and TMV-PDA with different reaction mass ratios of TMV:dopamine: (C1–2) 2:2.5 and (D1–2) 2:3.5. TEM of (E1–2) Gd-TMV and Gd-TMV-PDA with different mass ratios of Gd-TMV :

Author Manuscript Author Manuscript Author Manuscript Author Manuscript

dopamine: (F1–2) 2:2.5, (G1–2) 2:3.5, (H1–2) 2:5, and (I1–2) 2:7. Scale bar = 200 nm (B1-I1) and 100 nm (B2-I2).

Author Manuscript Author Manuscript Author Manuscript Author Manuscript

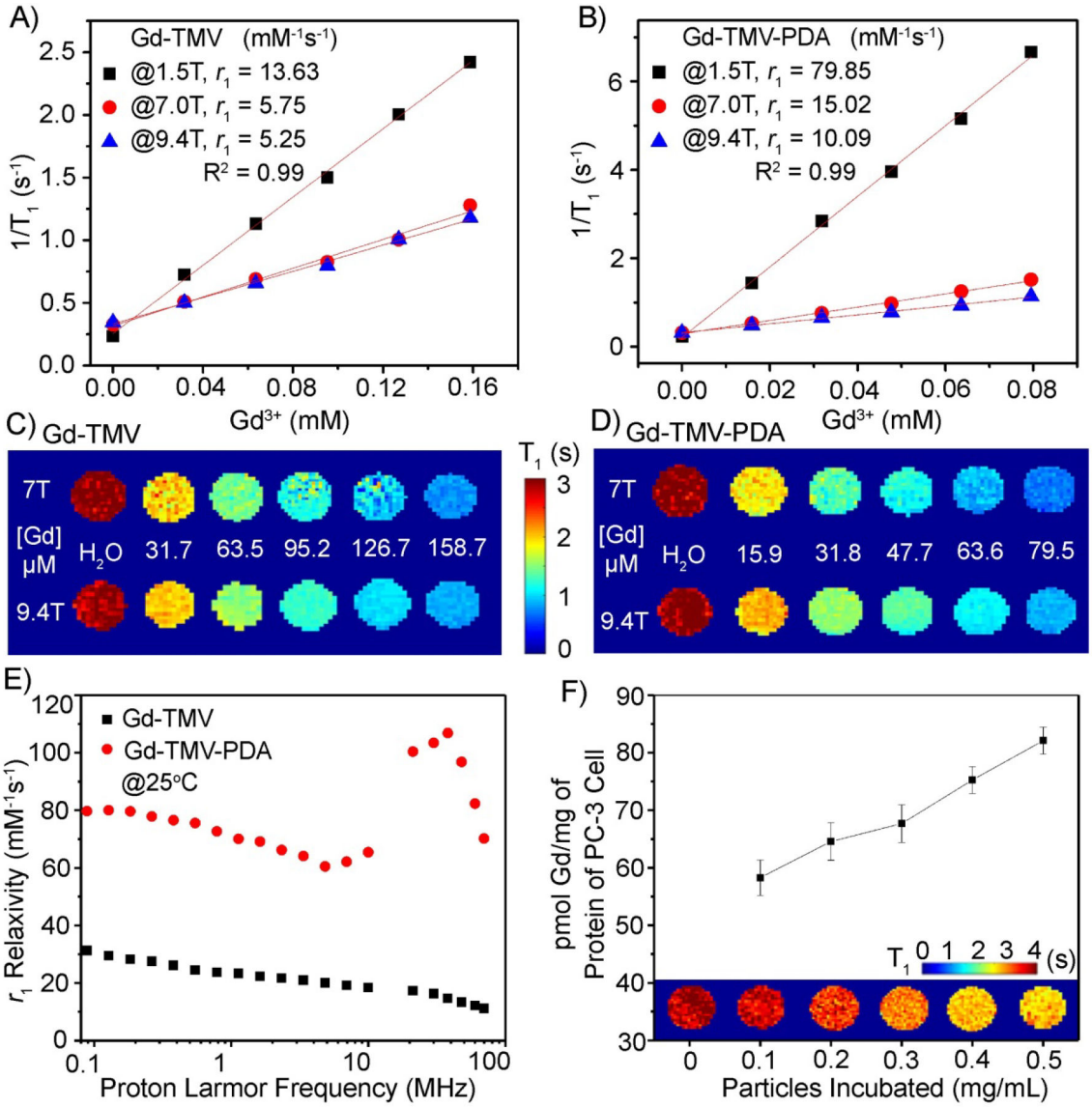

Fig. 2.

Water proton longitudinal (r_1) relaxation of (A) Gd-TMV and (B) Gd-TMV-PDA as a function of Gd^{3+} concentration measured at 37°C in magnetic fields of 1.5, 7.0 and 9.4 T. The T_1 mapping phantoms of (C) Gd-TMV and (D) Gd-TMV-PDA in aqueous solutions at various concentrations of Gd^{3+} in magnetic fields of 7.0 and 9.4 T. (E) The r_1 nuclear magnetic relaxation dispersion (NMRD) profiles (0.01–70 MHz) were obtained for the aqueous suspensions of Gd-TMV (■) and Gd-TMV-PDA (●) at 25°C normalized to 1 mM Gd^{3+}. (F) The *in vitro* T_1-mapping of PC-3 cells taking up different concentrations of Gd-TMV-PDA at 37°C for 3 h. Corresponding quantities of Gd^{3+} taken up by PC-3 cells were determined by ICP-OES and the Bradford protein assay following MRI.

Author Manuscript Author Manuscript Author Manuscript Author Manuscript

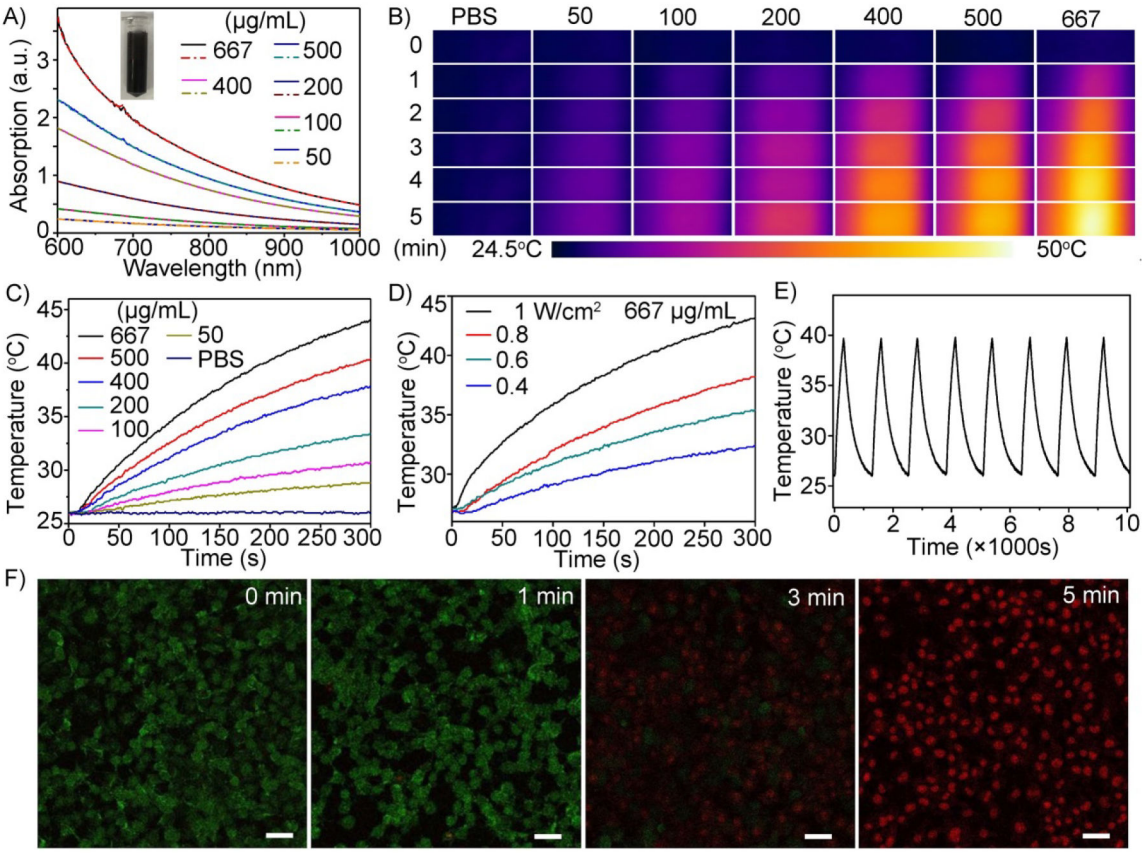

Fig. 3.

(A) Absorption spectra of Gd-TMV-PDA at different concentrations before (solid line) and after (dashed line) irradiation (808 nm laser, 1 W/cm^2). Inset shows a picture of the 200 μg/mL Gd-TMV-PDA solution. (B) Thermal images of different concentrations (50–667 μg/mL) of Gd-TMV-PDA irradiated for different durations (808 nm laser, 1 W/cm^2) recorded with an IR camera, and (C) the corresponding temperature change profiles. (D) Temperature profiles and thermal images of 667 μg/mL Gd-TMV-PDA solution irradiated with an 808-nm laser at different power densities (0.4–1 W/cm^2). (E) Temperature variations of a Gd-TMV-PDA over eight cycles of heating and natural cooling. (F) Confocal fluorescence images of live (calcein-AM: green)/dead (propidium iodide: red) PC-3 cells treated with Gd-TMV-PDA before and after irradiation (808 nm laser, 1 W/cm^2) for different durations (1–5 min). Scale bar = 50 μm.

Author Manuscript

Author Manuscript

Author Manuscript

Author Manuscript

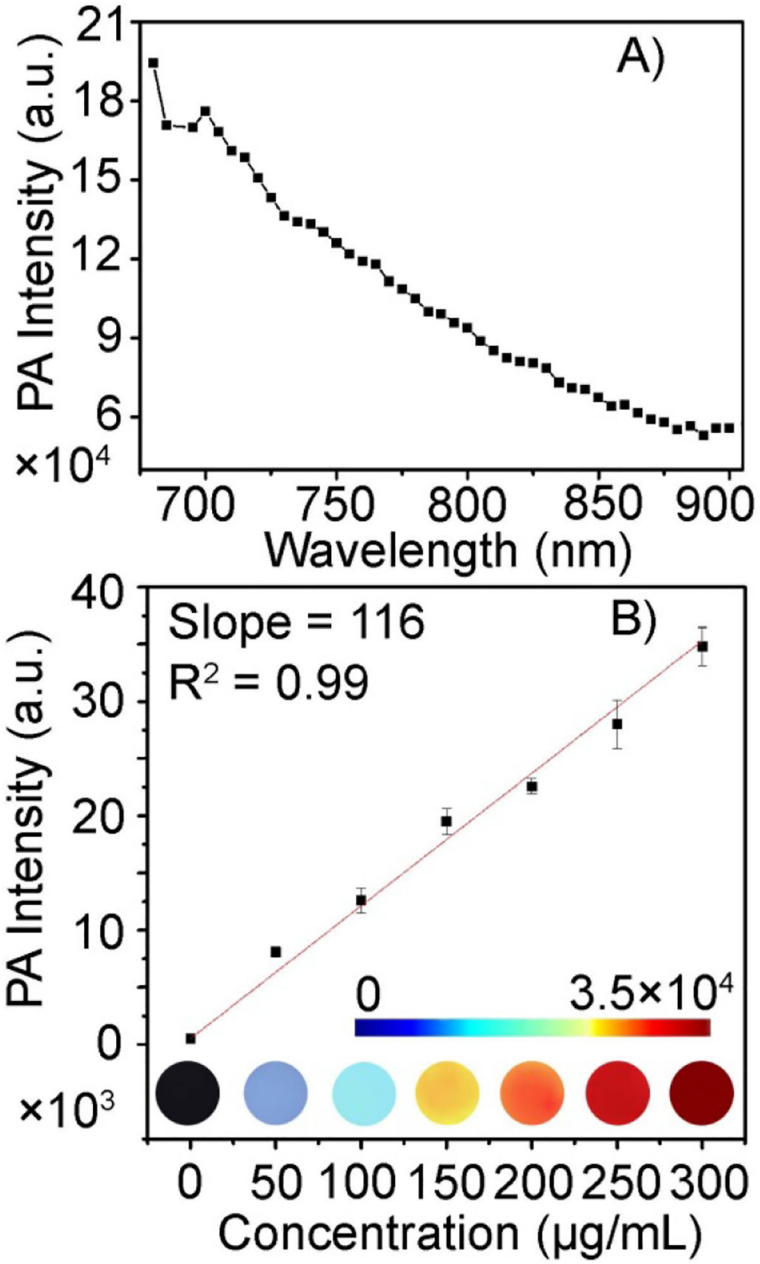

Fig. 4.

(A) The photoacoustic (PA) spectrum of Gd-TMV-PDA (200 μg/mL aqueous solution) scanned over the wavelength range 680–900 nm. (B) PA imaging phantoms and corresponding liner relationship between the PA signal intensity and concentration of Gd-TMV-PDA irradiated using a 680-nm pulsed laser.